

# Measurement of $\bar{\nu}_e$ -Electron Scattering Cross-Section with a CsI(Tl) Scintillating Crystal Array at the Kuo-Sheng Nuclear Power Reactor

M. Deniz,<sup>1,2</sup> S.T. Lin,<sup>1</sup> V. Singh,<sup>1,3</sup> J. Li,<sup>1,4,5</sup> H.T. Wong,<sup>1,\*</sup> S. Bilmis,<sup>1,2</sup> C.Y. Chang,<sup>1,6</sup> H.M. Chang,<sup>1</sup> W.C. Chang,<sup>1</sup> C.P. Chen,<sup>1</sup> M.H. Chou,<sup>1</sup> K.J. Dong,<sup>7</sup> J.M. Fang,<sup>8</sup> C.H. Hu,<sup>9</sup> G.C. Jon,<sup>1</sup> W.S. Kuo,<sup>9</sup> W.P. Lai,<sup>1</sup> F.S. Lee,<sup>1</sup> S.C. Lee,<sup>1</sup> H.B. Li,<sup>1</sup> H.Y. Liao,<sup>1</sup> C.W. Lin,<sup>1</sup> F.K. Lin,<sup>1</sup> S.K. Lin,<sup>1</sup> Y. Liu,<sup>1,4</sup> J.F. Qiu,<sup>1,4</sup> M. Serin,<sup>2</sup> H.Y. Sheng,<sup>1,4</sup> L. Singh,<sup>1,3</sup> R.F. Su,<sup>8</sup> W.S. Tong,<sup>9</sup> J.J. Wang,<sup>1</sup> P.L. Wang,<sup>1,4</sup> S.C. Wu,<sup>1,10</sup> S.W. Yang,<sup>1</sup> C.X. Yu,<sup>11</sup> Q. Yue,<sup>5</sup> M. Zeyrek,<sup>2</sup> D.X. Zhao,<sup>1,4</sup> Z.Y. Zhou,<sup>7</sup> Y.F. Zhu,<sup>1,5</sup> and B.A. Zhuang<sup>1,4</sup>

(TEXONO Collaboration)

<sup>1</sup> *Institute of Physics, Academia Sinica, Taipei 11529, Taiwan.*

<sup>2</sup> *Department of Physics, Middle East Technical University, Ankara 06531, Turkey.*

<sup>3</sup> *Department of Physics, Banaras Hindu University, Varanasi 221005, India.*

<sup>4</sup> *Institute of High Energy Physics, Chinese Academy of Science, Beijing 100039, China.*

<sup>5</sup> *Department of Engineering Physics, Tsing Hua University, Beijing 100084, China.*

<sup>6</sup> *Department of Physics, University of Maryland, College Park MD 20742, U.S.A.*

<sup>7</sup> *Department of Nuclear Physics, Institute of Atomic Energy, Beijing 102413, China.*

<sup>8</sup> *Kuo-Sheng Nuclear Power Station, Taiwan Power Company, Kuo-Sheng 207, Taiwan.*

<sup>9</sup> *Institute of Nuclear Energy Research, Lung-Tan 325, Taiwan.*

<sup>10</sup> *National Instruments, Taipei 106, Taiwan.*

<sup>11</sup> *Department of Physics, Nankai University, Tianjin 300071, China.*

(Dated: December 19, 2009)

The  $\bar{\nu}_e - e^-$  elastic scattering cross-section was measured with a CsI(Tl) scintillating crystal array having a total mass of 187 kg. The detector was exposed to a reactor  $\bar{\nu}_e$  flux of about  $6.4 \times 10^{12} \text{ cm}^{-2}\text{s}^{-1}$  at the Kuo-Sheng Nuclear Power Station. The experimental design, conceptual merits, detector hardware, data analysis and background understanding of the experiment are presented. Using 29882/7369 kg-days of Reactor ON/OFF data, the Standard Model (SM) electroweak interaction was probed at the squared 4-momentum transfer range of  $Q^2 \sim 3 \times 10^{-6} \text{ GeV}^2$ . The ratio of experimental to SM cross-sections of  $\xi = [1.08 \pm 0.21(\text{stat}) \pm 0.16(\text{sys})]$  was measured. Constraints on the electroweak parameters ( $g_V, g_A$ ) were placed, corresponding to a weak mixing angle measurement of  $\sin^2\theta_W = 0.251 \pm 0.031(\text{stat}) \pm 0.024(\text{sys})$ . Destructive interference in the SM  $\bar{\nu}_e - e^-$  process was verified. Bounds on anomalous neutrino electromagnetic properties were placed: neutrino magnetic moment at  $\mu_{\bar{\nu}_e} < 2.2 \times 10^{-10} \mu_B$  and the neutrino charge radius at  $-2.1 \times 10^{-32} \text{ cm}^2 < \langle r_{\bar{\nu}_e}^2 \rangle < 3.3 \times 10^{-32} \text{ cm}^2$ , both at 90% confidence level.

PACS numbers: 14.60.Lm, 13.15.+g, 25.30.Pt.

## 1. INTRODUCTION

The compelling evidence of neutrino oscillations from the solar, atmospheric as well as long baseline accelerator and reactor neutrino measurements implies finite neutrino masses and mixings [1]. Their physical origin and experimental consequences are not fully understood. Experimental studies on the neutrino properties and interactions are crucial because they can shed light to these fundamental questions and may provide hints or constraints to models on new physics.

We report a study of neutrino-electron scattering using reactor neutrinos at the Kuo-Sheng Nuclear Power Station with a CsI(Tl) scintillating crystal array. The cross-section formulae are summarized in Section 2. The conceptual design, hardware construction and performance are presented in Section 3, followed by discussions on event reconstruction, background understanding and suppression, as well as experimental systematic effects. Section 7 shows results on the Standard Model (SM) electroweak physics [2] as well as constraints on possi-

ble neutrino electromagnetic interactions.

## 2. NEUTRINO-ELECTRON SCATTERING

Neutrino-electron scattering has been studied with several generations of experiments at the accelerator using mostly muon-neutrinos  $\nu_\mu(\bar{\nu}_\mu)$  [3, 4]. It is a pure leptonic process and therefore provides a clean test to SM. The typical squared 4-momentum transfer was  $Q^2 \sim 10^{-2} \text{ GeV}^2$  and the electroweak angle  $\sin^2\theta_W$  was probed to an accuracy of  $\pm 3.6\%$ .

Using electron-neutrinos as probe, the interaction

$$\nu_e(\bar{\nu}_e) + e^- \rightarrow \nu_e(\bar{\nu}_e) + e^- \quad (1)$$

has been studied at medium energy accelerators [5, 6] as well as at the power reactors [7–10]. It is also an important channel in the detection of solar neutrinos [11] where the SM  $\nu_e - e^-$  scattering cross-section was used to extract neutrino oscillation parameters. This process is among the few of the SM interactions which proceed via

TABLE I: Summary of published  $\nu_e$ - and  $\bar{\nu}_e$ - $e$  scattering cross-section and  $\sin^2\theta_W$  measurements. Unavailable entries are denoted by “N/A”.

Experiment	$E_\nu$ (MeV)	T (MeV)	Events [14]	Published Cross-Section	$\sin^2\theta_W$
<u>Accelerator <math>\nu_e</math> :</u>					
LAMPF [5]	$7 < E_\nu < 50$	7–50	236	$[10.0 \pm 1.5 \pm 0.9] \cdot E_\nu$ $\times 10^{-45} \text{ cm}^2$	$0.249 \pm 0.063$
LSND [6]	$20 < E_\nu < 50$	20–50	191	$[10.1 \pm 1.1 \pm 1.0] \cdot E_\nu$ $\times 10^{-45} \text{ cm}^2$	$0.248 \pm 0.051$
<u>Reactor <math>\bar{\nu}_e</math> :</u>					
Savannah River					
Original [7]	$\left\{ \begin{array}{l} 1.5 < E_\nu < 8.0 \\ 3.0 < E_\nu < 8.0 \end{array} \right.$	1.5–3.0	381	$[0.87 \pm 0.25] \cdot \sigma_{V-A}$	$\left. \right\} 0.29 \pm 0.05$
		3.0–4.5	77	$[1.70 \pm 0.44] \cdot \sigma_{V-A}$	
Re-analysis [13]	$\left\{ \begin{array}{l} 1.5 < E_\nu < 8.0 \\ 3.0 < E_\nu < 8.0 \end{array} \right.$	1.5–3.0	N/A	$[1.35 \pm 0.4] \cdot \sigma_{SM}$	$\left. \right\} \text{N/A}$
		3.0–4.5	N/A	$[2.0 \pm 0.5] \cdot \sigma_{SM}$	
Krasnoyarsk [8]	$3.2 < E_\nu < 8.0$	3.2–5.2	N/A	$[4.5 \pm 2.4]$ $\times 10^{-46} \text{ cm}^2/\text{fission}$	$0.22^{+0.7}_{-0.8}$
Rovno [9]	$0.6 < E_\nu < 8.0$	0.6–2.0	41	$[1.26 \pm 0.62]$ $\times 10^{-44} \text{ cm}^2/\text{fission}$	N/A
MUNU [10]	$0.7 < E_\nu < 8.0$	0.7–2.0	68	$[1.07 \pm 0.34] \text{ events/day}$	N/A
TEXONO (This Work)	$3.0 < E_\nu < 8.0$	3.0–8.0	$\sim 414$	$[1.08 \pm 0.21 \pm 0.16] \cdot \sigma_{SM}$	$0.251 \pm 0.031 \pm 0.024$

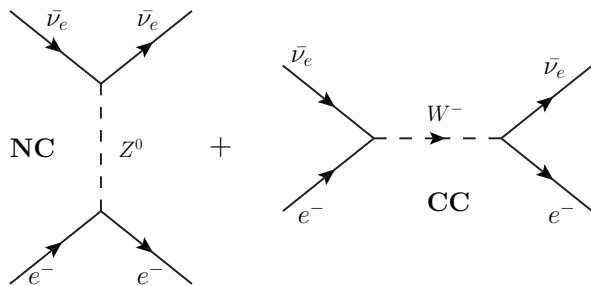


FIG. 1: Interactions of  $\bar{\nu}_e$  with electron via the SM-allowed charged current (CC) and neutral current (NC) channels. There is in addition interference effect between them.

charged current (CC), neutral current (NC) as well as their interference (Int) [12], as illustrated schematically in Figure 1. The interference effect in  $\nu_e$ - $e$  scattering is the origin of matter oscillation of solar neutrinos in the interior of the Sun [1].

The experimental results on  $\nu_e$ - and  $\bar{\nu}_e$ - $e$  scattering are summarized in Table I. Neutrino-electron scattering was first observed with reactor reactors in the Savannah River experiment [7]. Re-analysis of the data by a later work [13] with improved input on the reactor neutrino spectra and electroweak parameters gave cross-sections which were  $\sim 2\sigma$  higher than the SM values. The discrepancies were interpreted as hints of anomalous neutrino interactions. Other subsequent experiments [8–10] focused on the searches of neutrino magnetic moments at low recoil energy such that their sensitivities to SM physics were limited.

## 2.1 Electroweak Parameters

The SM differential cross-section in the laboratory frame for  $\nu_\mu(\bar{\nu}_\mu)$ - $e$  elastic scattering, where only NC is involved, is given by [2, 3];

$$\left[ \frac{d\sigma}{dT}(\bar{\nu}_\mu e) \right]_{SM} = \frac{G_F^2 m_e}{2\pi} \cdot [ (g_V \pm g_A)^2 + (g_V \mp g_A)^2 \left( 1 - \frac{T}{E_\nu} \right)^2 - (g_V^2 - g_A^2) \frac{m_e T}{E_\nu^2} ] \quad , \quad (2)$$

where  $G_F$  is the Fermi coupling constant,  $T$  is the kinetic energy of the recoil electron,  $E_\nu$  is the incident neutrino energy and  $g_V$ ,  $g_A$  are, respectively, the vector and axial-vector coupling constants. The upper(lower) sign refers to the interactions with  $\nu_\mu(\bar{\nu}_\mu)$ . For  $\nu_e(\bar{\nu}_e)$ - $e$  scattering, all CC, NC and Int are involved [12], and the cross-section can be obtained by making the replacement  $g_{V,A} \rightarrow (g_{V,A} + 1)$ . In the case of  $\bar{\nu}_e$ - $e$  which is relevant for reactor neutrinos,

$$\left[ \frac{d\sigma}{dT}(\bar{\nu}_e e) \right]_{SM} = \frac{G_F^2 m_e}{2\pi} \cdot [ (g_V - g_A)^2 + (g_V + g_A + 2)^2 \left( 1 - \frac{T}{E_\nu} \right)^2 - (g_V - g_A)(g_V + g_A + 2) \frac{m_e T}{E_\nu^2} ] \quad . \quad (3)$$

The SM assignments to the coupling constants are:

$$g_V = -\frac{1}{2} + 2 \sin^2 \theta_W \quad \text{and} \quad g_A = -\frac{1}{2} \quad , \quad (4)$$

where  $\sin^2\theta_W$  is the weak mixing angle. The SM differential cross-section expressed in terms of  $\sin^2\theta_W$  is accordingly:

$$\left[\frac{d\sigma}{dT}(\bar{\nu}_e e)\right]_{SM} = \frac{G_F^2 m_e}{2\pi} \cdot \left\{ 4 (\sin^2\theta_W)^2 \left[ 1 + \left(1 - \frac{T}{E_\nu}\right)^2 - \frac{m_e T}{E_\nu^2} \right] + 4 \sin^2\theta_W \left[ \left(1 - \frac{T}{E_\nu}\right)^2 - \frac{m_e T}{2E_\nu^2} \right] + \left(1 - \frac{T}{E_\nu}\right)^2 \right\} . \quad (5)$$

The observables in an experiment are the event rates ( $R_{expt}$ ). The SM predicted rate, expressed in unit of  $\text{kg}^{-1}\text{day}^{-1}$ , can be written as

$$R_{SM}(\nu) = \rho_e \int_T \int_{E_\nu} \left[\frac{d\sigma}{dT}\right]_{SM} \frac{d\phi}{dE_\nu} dE_\nu dT , \quad (6)$$

where  $\rho_e$  is the electron number density per kg of target mass, and  $d\phi_\nu/dE_\nu$  denotes the neutrino spectrum.

Results of this work are reported in several schemes using  $R_{expt}$ . Firstly, the cross-section ratio

$$\xi = \frac{R_{expt}(\nu)}{R_{SM}(\nu)} \quad (7)$$

can be used to probe new physics in a model-independent way. Alternatively, taking SM electroweak interactions but allowing the parameters to assume any values, the allowed ranges of  $(g_V, g_A)$  as well as  $\sin^2\theta_W$  can be derived from  $R_{expt}$ , following Eqs. 3&5, respectively.

To study the interference effects, the measured rate can be expressed as

$$R_{expt} = R_{CC} + R_{NC} + \eta \cdot R_{Int} . \quad (8)$$

The CC–NC interference for  $\nu_e(\bar{\nu}_e)$ –e is destructive in SM, or equivalently  $\eta(SM) = -1$ . Possible deviations in the sign and magnitude of the interference effects ( $\eta$ ) can be probed.

It follows from Eqs. 5&6 and the analogous formulae for  $\nu_e$ –e that, under realistic experimental configurations, the projected accuracies on  $\sin^2\theta_W$  (denoted by  $\Delta[\sin^2\theta_W]$ ) are related to the experimental uncertainties in  $\xi$  (denoted by  $\Delta[\xi]$ ) by:

$$\Delta[\sin^2\theta_W] \sim \left\{ \begin{array}{l} 0.15 \cdot \Delta[\xi(\bar{\nu}_e e)] \\ 0.35 \cdot \Delta[\xi(\nu_e e)] \end{array} \right\} \quad (9)$$

for reactor  $\bar{\nu}_e$ –e (this work) and accelerator  $\nu_e$ –e [5, 6] experiments, respectively. Accordingly, the studies of reactor  $\bar{\nu}_e$ –e are expected to improve on the sensitivities of  $\sin^2\theta_W$  and  $(g_V, g_A)$  at the same experimental accuracies as those from  $\nu_e$ –e measurements. The relative strength

of the three components normalized to  $R_{expt} = 1$  are in the ratios of

$$(R_{CC} : R_{NC} : R_{Int}) \sim \left\{ \begin{array}{l} (0.77 : 0.92 : 0.69) \text{ for } \bar{\nu}_e - e \\ (1.77 : 0.16 : 0.93) \text{ for } \nu_e - e \end{array} \right. . \quad (10)$$

The stronger NC component in  $\bar{\nu}_e$ –e scattering is the physical basis of the sensitivity enhancement in the derivation of  $\sin^2\theta_W$ .

The SM was tested and  $\sin^2\theta_W$  was precisely measured in the high energy ( $Q^2 > \text{GeV}^2$ ) region with accelerator experiments on  $e^+e^-$ , polarized  $ep$  and  $\nu N$  deep inelastic processes, and in the low energy ( $Q^2 < 10^{-6} \text{GeV}^2$ ) region with measurements on atomic parity violation [2]. Among them, the  $\sin^2\theta_W$  derived from the NuTeV experiment on  $\nu N$  deep inelastic scattering [15] was  $3\sigma$  higher than SM prediction, though the interpretations were complicated by strong interaction effects [2]. Destructive interference according to SM prediction has been demonstrated by accelerator  $\nu_e$ –e scattering experiments [5, 6].

The objective of this work is to bridge the  $Q^2$  gap in probing SM electroweak physics with reactor  $\bar{\nu}_e$ –e interactions. In particular, the interference effects are studied in this unique system. This would complement the precision data obtained at accelerator at higher  $Q^2$ . The measurements would place constraints on various anomalous neutrino interactions such as those discussed in the next section.

## 2.2 Neutrino Electromagnetic Properties

The neutrino electromagnetic interactions [17] provide natural extensions to SM. The relevant parameters are  $\langle r_{\bar{\nu}_e}^2 \rangle$  [14], usually called the “neutrino charge radius”, and neutrino magnetic moments ( $\mu_\nu$ ) [18] which describe possible neutrino interactions with matter via the exchange of virtual photons without and with the change of its helicity.

Interpretations of  $\langle r_{\bar{\nu}_e}^2 \rangle$  remain controversial. A straight-forward definition has been shown to be gauge-dependent and hence  $\langle r_{\bar{\nu}_e}^2 \rangle$  is unphysical [19]. However, there are recent attempts to define a physical observable with  $\langle r_{\bar{\nu}_e}^2 \rangle$  [20], which give a predicted value of  $\langle r_{\bar{\nu}_e}^2 \rangle = 0.4 \times 10^{-32} \text{cm}^2$  with the SM framework. We adopt in this article the more general interpretation that  $\langle r_{\bar{\nu}_e}^2 \rangle$  parametrizes contributions to non-standard interactions in neutrino scattering [21].

Changes to the SM cross-sections due to  $\langle r_{\bar{\nu}_e}^2 \rangle$  can be obtained from Eq. 5 via the replacement [13]:

$$\sin^2\theta_W \rightarrow \sin^2\theta_W + \left(\frac{\sqrt{2}\pi\alpha_{em}}{3G_F}\right)\langle r_{\bar{\nu}_e}^2 \rangle , \quad (11)$$

where  $\alpha_{em}$  is the fine structure constant.

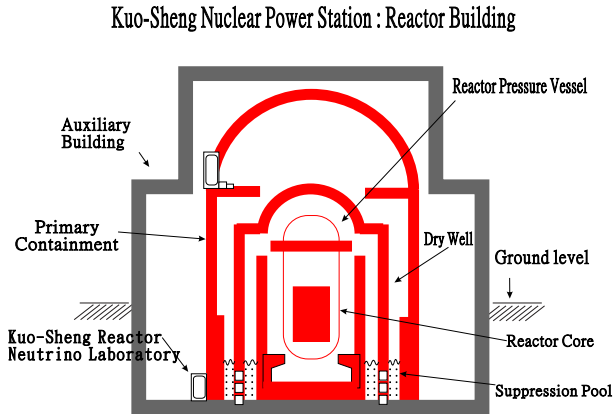


FIG. 2: Schematic layout of the Kuo-Sheng Neutrino Laboratory together with the reactor core and building.

Contributions of  $\mu_\nu$  can be described by an additional term to Eqs. 3&5:

$$\left(\frac{d\sigma}{dT}\right)_{\mu_\nu} = \frac{\pi\alpha_{em}^2\mu_\nu^2}{m_e^2} \left[\frac{1 - T/E_\nu}{T}\right]. \quad (12)$$

The SM prediction of  $\mu_\nu$  for massive Dirac neutrinos is extremely small ( $3.2 \times 10^{-19} \mu_B$  where  $\mu_B$  is the Bohr magneton). However, various models with Majorana neutrinos can give rise to  $\mu_\nu$  at the range of  $(10^{-10} - 10^{-13}) \mu_B$  relevant to experiments and astrophysics [18]. The most sensitive direct laboratory limits on  $\mu_\nu$  come from high-purity germanium detectors at  $\sim 10$  keV threshold with reactor  $\bar{\nu}_e$  [16, 22]. At this low recoil energy, the  $\mu_\nu$  contributions at the present limit are orders of magnitude larger than those due to SM  $\bar{\nu}_e$ -e cross-sections.

### 3. EXPERIMENTAL SET-UP

#### 3.1 Laboratory Facilities and Neutrino Flux

A research program on low energy neutrino physics [23] is being pursued by the TEXONO Collaboration at the Kuo-Sheng Neutrino Laboratory (KSNL), which is located at a distance of 28 m from Core #1 of the Kuo-Sheng Nuclear Power Station in Taiwan. A schematic diagram is depicted in Figure 2. The site is at the ground floor of the reactor building at a depth of 10 m below ground level, with an overburden of  $\sim 30$  meter-water-equivalence. The nominal thermal power output is 2.9 GW. The standard operation includes  $\sim 18$  months of Reactor ON periods separated by  $\sim 50$  days of Reactor outage OFF periods when typically one-third of the fuel elements are replaced.

A summary of the key information on the four data taking periods reported in this article is given in Table II.

The evaluation of the reactor neutrino flux and spectra was discussed in details in Refs. [16, 24]. The total  $\bar{\nu}_e$ -flux at KSNL is about  $6.4 \times 10^{12} \text{ cm}^{-2}\text{s}^{-1}$ . A typical spectrum is displayed in Figure 3. It has been demonstrated through  $\bar{\nu}_e$ -proton measurements that the integrated  $\bar{\nu}_e$ -flux for  $E_\nu > 1.8$  MeV [25] and  $\bar{\nu}_e$ -spectra for  $E_\nu > 3$  MeV [26] agreed with calculations to better than  $< 3\%$  and  $< 5\%$ , respectively.

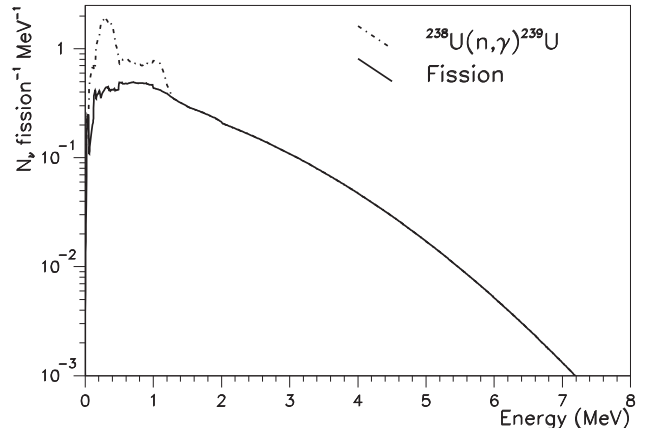


FIG. 3: Total  $\bar{\nu}_e$  spectrum at typical power reactor operation.

The laboratory is equipped with a 50-ton shielding structure depicted schematically in Figure 4, consisting of, from outside in, 2.5 cm thick plastic scintillator panels with photo-multiplier tubes (PMTs) readout for cosmic-ray veto, 15 cm of lead, 5 cm of stainless steel support structures, 25 cm of boron-loaded polyethylene and 5 cm of Oxygen Free High Conductivity (OFHC) copper. The inner target volume with a dimension of  $100 \times 80 \times 75 \text{ cm}^3$  allows different detectors for various physics topics to be placed. Data were taken with a CsI(Tl) scintillating crystal array during data acquisition (DAQ) periods II–V. Each period consisted of both reactor ON and OFF data taking.

#### 3.2 Conceptual Design and Motivations

The merits of scintillating crystal detectors in generic low background low energy experiments have been discussed [27]. This experiment adopted CsI(Tl) crystal scintillator packed in a compact array as both target and detector. A schematic layout is given in Figure 5. Several detector characteristics and design features were incorporated [28] which contributed to the improvement in the experimental sensitivities:

1. **Proton-Free Target Region:** The CsI(Tl) crystal is only weakly hygroscopic and does not require a hermetic container to seal it from ambient humidity (in contrast to NaI(Tl) crystal). The crys-

TABLE II: Summary of the key information of the four data taking periods. The period numbering follows the same scheme as in Ref [16] .

Period	Data Taking Calendar Time	Reactor ON Live Time (days)	Reactor OFF Live Time (days)	DAQ Live Time (%)	DAQ Threshold (keV)	Average $\bar{\nu}_e$ Flux ( $10^{12} \text{cm}^{-2} \text{s}^{-1}$ )	Fiducial Mass (kg)
II	Feb. 2003 - Oct. 2003	95.2	48.4	88.8	$\sim 100$	6.27	43.5
III	Sept. 2004 - Oct. 2005	192	36.6	93.4	$\sim 500$	6.50	40.5
IV	Mar. 2006 - May 2007	204.9	43.5	88.0	$\sim 500$	6.44	51
V	June 2007 - Feb. 2008	132.8	27.6	91.9	$\sim 500$	6.29	57
Combined	Feb. 2003 - Feb. 2008	624.9	156.1	90.4	—	6.39	—

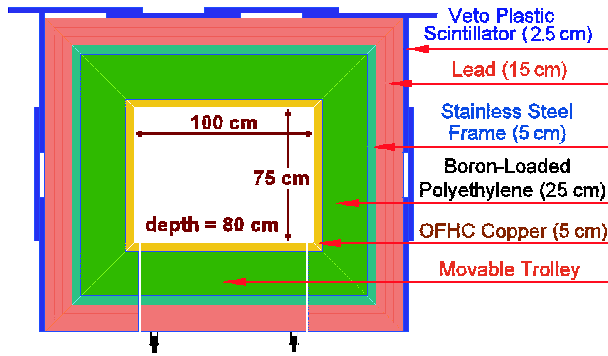


FIG. 4: The shielding design of KSNL. Similar structures apply to the back and front walls. Detectors and inner shieldings were placed in the inner target volume.

tal is also mechanically stable and self-supporting. Therefore, the target region was made up almost entirely of CsI(Tl) (equal amount of Cs and I, with 0.15% admixture of Tl). The other materials were the small amount of teflon wrapping sheets, made up of C and F and contributing to only about 0.13% by mass. There were no protons, such that possible neutrino-induced background from  $\bar{\nu}_e - p$  was eliminated. The cross-section of this interaction is  $>10^2$  times higher than that of  $\bar{\nu}_e - e$ . This background could not be suppressed with Reactor ON/OFF comparisons, and could be a potential problem with the Savannah River experiment [7] where plastic scintillators were adopted as target.

2. **Completely Active Fiducial Volume:** The absence of detector housing allowed a fiducial volume which was totally active. The probability of background events to be completely measured was enhanced, and this was beneficial to background understanding and suppression.
3. **Complete Three-Dimensional Reconstruction:** Each CsI(Tl) crystal module consisted of a hexagonal-shaped cross-section with 2 cm side and a length of 40 cm, giving a modular mass of 1.87 kg. Scintillation photons were read out by PMTs at

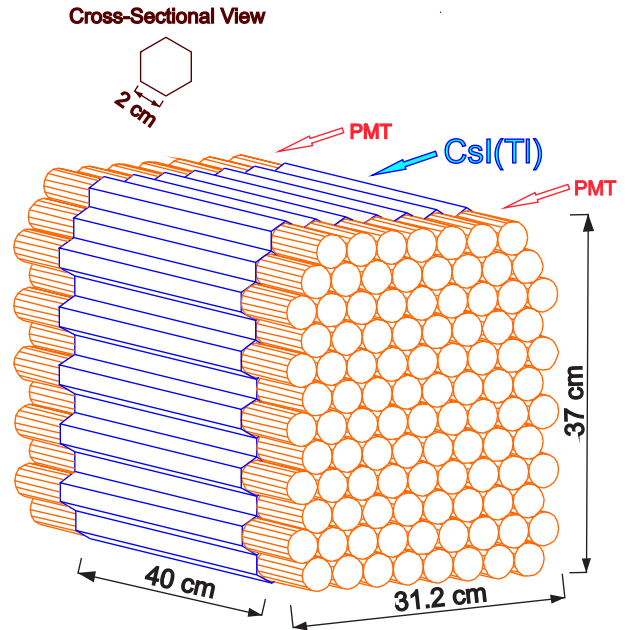


FIG. 5: Schematic drawing of the CsI(Tl) scintillating crystal array. Light output is recorded by PMTs at both ends.

both ends. The sum and difference of the two signals provided the energy and position information, respectively. A three-dimensional reconstruction of the events was achieved. These information greatly enhanced the capabilities of background diagnostics and evaluation. In particular, background induced by ambient radiations was suppressed by rejecting events at the outer modules or close to the PMTs. The high atomic number for Cs and I ( $Z=51$  and  $53$ , respectively) allowed efficient attenuation and therefore compact detector geometry.

4. **Large Mass and Expandable Detector:** This experiment was based on a modular CsI(Tl) crystal array with a total mass of 187 kg. Such detector approach with similar target mass scale was also adopted in cold dark matter searches in the KIMS experiment [29]. The design can be easily expanded to ton-scale experiments and beyond.

5. **Pulse Shape Discrimination:** The light emission profiles of CsI(Tl) offered excellent pulse shape discrimination (PSD) between  $\gamma/e$  events from those due to  $\alpha$ -particles and nuclear recoils [30, 31]. This allowed precise measurements of the internal contaminations for background suppression and diagnostics.
6. **Focus at High Energy Events:** The reactor  $\bar{\nu}_e$ -spectra below 2 MeV has large uncertainties [24], while ambient background dominate below the natural radioactivity end-point of 2.6 MeV. Accordingly, only events with  $T > 3$  MeV were studied as potential  $\bar{\nu}_e$ -e candidates. The low energy events were still recorded and analyzed for the purposes of calibrations and background diagnostics.

### 3.3 Detector Construction and Readout

As depicted in Figure 5, the scintillating CsI(Tl) crystal detector modules were packed into a matrix array, with minimal inactive dead space due to the teflon wrapping sheets. The configurations varied between the different DAQ periods, but the operation conditions were kept uniform and stable within one period. Therefore, each DAQ period can be taken as an independent experiment. At the end of data taking, a  $12 \times 9$  array was deployed giving a total mass of 187 kg. Fiducial volume was defined to be the inner crystals with a separation of  $>4$  cm from the PMTs at both ends. The fiducial masses for individual periods are given in Table II.

There were two types of crystal modules [30] from two production batches: (a) single crystal with 40 cm length were used as target placed in the central region, while (b) two pieces of 20 cm long crystals optically glued together were placed in the outer layers as active veto. The light output was read out at both ends of the crystal modules by custom designed PMTs with low-activity glass and diameter of 29 mm. The target array was housed inside a OFHC copper box of thickness 2.5 mm. Additional copper shielding blocks were placed on top of the box to fill up the inner target volume of Figure 4. The box was flushed with dry nitrogen to purge the radioactive radon gas. The CsI(Tl) array shared the target volume and the downstream DAQ systems with germanium detectors for magnetic moment studies [16] and dark matter searches [32].

The electronics and DAQ systems were described in Ref. [33]. The DAQ system was VME-based running on LINUX operating system. The PMT signals were fed to custom-built shaping amplifiers whose output were recorded by Flash Analog-to-Digital Converter (FADC) modules at a clock rate of 20 MHz and 8-bit dynamic range. The DAQ trigger was generated by discriminator set at threshold of  $\sim 100$  keV for P-II and  $\sim 500$  keV for

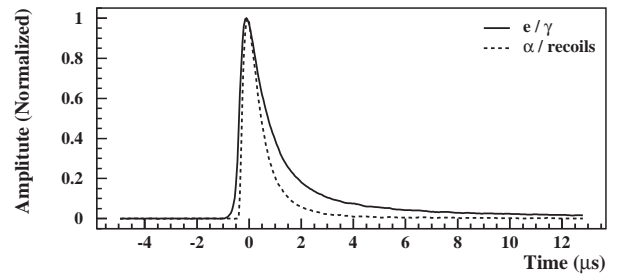


FIG. 6: Averaged pulse shapes due to 5.4 MeV  $\alpha$ -particles and  $\gamma$ -rays of 662 keV. Nuclear recoils, as measured with scattering with a neutron beam, give rise the same pulse shapes as the  $\alpha$ -events [30].

P-III,IV,V, much lower than the relevant signal region. Signals from all sub-dominant channels with energy depositions  $\gtrsim 10$  keV, as well as the PMT signals from the veto-panel system and various control parameters, were also recorded.

A special feature of the DAQ system was the recording of any events delayed as much as 500  $\mu$ s after the initial trigger. The delay time was measured with 1  $\mu$ s resolution. This allowed measurement of delayed-coincidence events due to internal radioactivity, which in turn was crucial to background diagnostics and suppression. The DAQ output was zero-suppressed, such that only those CsI(Tl) channels having signals within (-5  $\mu$ s, 500  $\mu$ s) relative to the trigger instant were recorded.

The DAQ dead time was accurately measured by the random trigger (RT) events generated at 0.1 Hz uncorrelated with the rest of the hardware. The typical trigger rate for the CsI(Tl) array was  $\sim 20$ – $30$  Hz, corresponding to  $\sim 8$ – $12\%$  of DAQ dead time. Data were taken with the germanium system in parallel in Periods II–IV, but the additional contributions to the DAQ dead time were only minor.

### 3.4 Detector Performance

The intrinsic performance of the CsI(Tl) crystal modules were discussed in details in Ref. [30]. The energy and position resolutions on individual module measured with a  $^{137}\text{Cs}$   $\gamma$ -source at 662 keV were 4% and  $<1$  cm root-mean-square (RMS), respectively. The averaged pulse shapes for  $\gamma/e$  events and  $\alpha$ -particles in CsI(Tl) are displayed in Figure 6. Separation of  $\gamma/\alpha$  at  $>99\%$  was achieved by PSD down to about 100 keV electron-equivalence energy.

The FADC has a hardware dynamic range of only 8-bit. Software algorithm was devised to correct the saturated pulse shapes [34]. The effective range was extended by 4 more bits without affecting the performance parameters like energy resolution and PSD. The CsI(Tl) out-

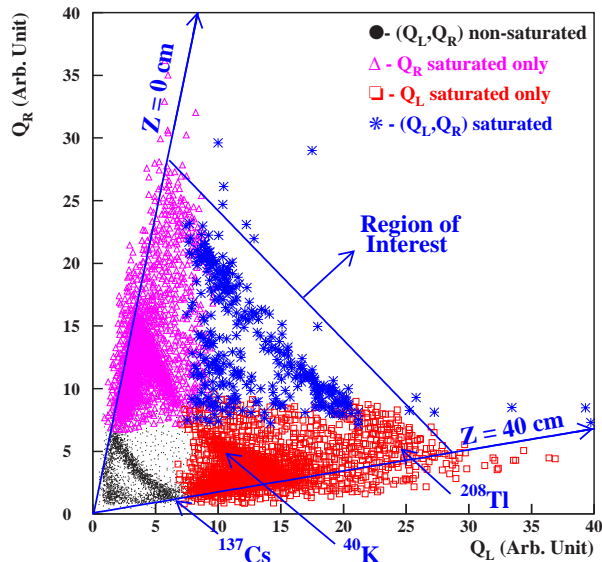


FIG. 7: Typical  $Q_L$  versus  $Q_R$  distribution for H1(CRV) events showing the background events of natural sources. Different colors denote whether the PMT signals are saturated at their FADC readout or not. Additional software routines were devised to provide correct energy information for saturated events.

put for the current measurements typically saturated at  $\sim 2$  MeV, so that the events with energy  $< 10$  MeV relevant to the analysis were well-reconstructed.

## 4. DATA ANALYSIS

### 4.1 Light Collection

The raw input to subsequent analysis were the light output (denoted by  $Q_L$  and  $Q_R$ ) derived by summing the pedestal-subtracted FADC signals from the PMTs on both ends of the CsI(Tl) modules. Depicted in Figure 7 is a typical normalized  $Q_L$  versus  $Q_R$  distribution. The selected events were those having signals only in one crystal (H1), with “cosmic-ray veto” (CRV) imposed and software correction applied to the saturated pulses [34]. The different color schemes denote the status on pulse saturation of the two PMTs.

Three bands along the increasing energy axis are conspicuous, corresponding to background due to  $\gamma$ -rays from  $^{137}\text{Cs}$  (662 keV),  $^{40}\text{K}$  (1461 keV) and  $^{208}\text{Tl}$  (2614 keV). These lines were important for *in situ* calibration as well as background diagnostics. The sharp reduction of background beyond the  $^{208}\text{Tl}$  energy – the signal region of this measurement – is very distinct. The enhanced event rates at both edges indicate that most background sources were external to the detector.

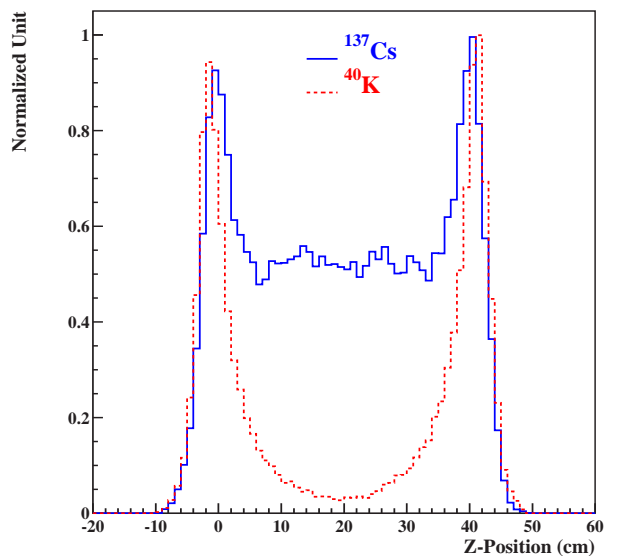


FIG. 8: The longitudinal Z-position distributions for events at energy corresponding to  $\gamma$ -lines of  $^{137}\text{Cs}$  (solid histogram) and  $^{40}\text{K}$  (dotted histogram).

### 4.2 Event Reconstruction

The objectives of event reconstruction were to provide measurements on energy (E) and longitudinal position (Z) using  $Q_L$  and  $Q_R$ . The calibration procedures were performed with *in situ* data, typically once every week.

The longitudinal Z-position for the  $i^{\text{th}}$  crystal module is given by:

$$Z \propto \left[ \frac{\beta_i \cdot Q_R - Q_L}{\beta_i \cdot Q_R + Q_L} \right], \quad (13)$$

where  $\beta_i$ 's are parameters to absorb the residual difference in response between the left and right readout. The values of  $\beta_i$ 's were obtained by requiring that the 662 keV  $\gamma$ -line from  $^{137}\text{Cs}$  background must be uniformly distributed along the length of the crystals. The proportional constants were derived by fixing the two edges of the distributions to be at 0 cm and 40 cm. Typical Z-position distributions for events at 662 keV and 1461 keV evaluated through this prescription are shown in Figure 8. The RMS resolution is about 1.3 cm at 3 MeV electron-equivalence, based on measurements with  $\alpha$ - $\alpha$  cascade events [35].

The energy is described by:

$$E = a_i + b_i \cdot e^{-\alpha_i Z} \cdot \sqrt{Q_L \times Q_R}. \quad (14)$$

The parameters  $\alpha_i$ 's take into account possible differences in the attenuation of light transmission along both directions, and were fixed by requiring the derived values of E for the  $\gamma$ -lines were constant and independent of Z. The calibration constants ( $a_i, b_i$ ) were evaluated by a linear fit to the  $\gamma$ -lines. The reconstructed energy spectra

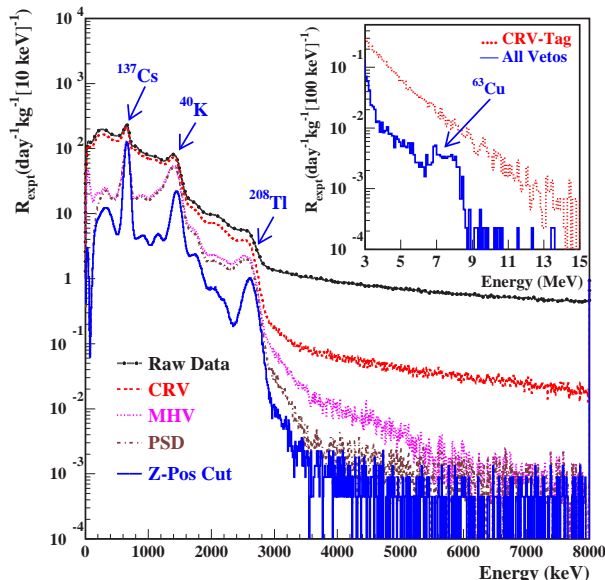


FIG. 9: The measured energy spectra at various stages of the analysis showing the effects of successive selection cuts.

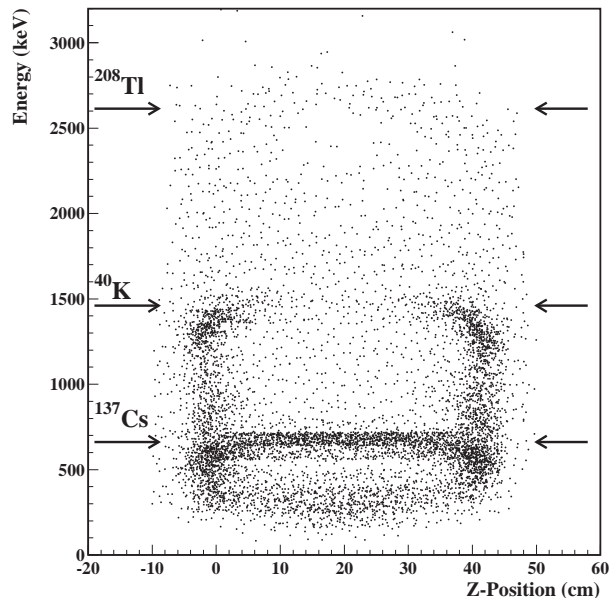


FIG. 10: Energy versus Z-position scatter plot of reconstructed events. The prominent  $\gamma$ -lines matching the various bands are identified.

are depicted in Figure 9, indicating RMS resolutions of 5.8%, 5.2% and 4.0% at  $^{137}\text{Cs}$ ,  $^{40}\text{K}$  and  $^{208}\text{Tl}$   $\gamma$ -peaks, respectively. A scatter plot of the reconstructed ( $E, Z$ ) values for a typical crystal is shown in Figure 10. The reconstructed energy of the various bands matched well to the corresponding  $\gamma$ -lines within the fiducial volume ( $4 \text{ cm} < Z < 36 \text{ cm}$ ).

TABLE III: Summary of the suppression and signal efficiency factors of successive selection cuts within the 3–8 MeV energy range.

Event Selection	Background Suppression	Signal Efficiency
Raw Data	1.0	1.0
Cosmic Ray Veto (CRV)	0.06	0.93
Multi-Hit Veto (MHV)	0.16	0.99
Pulse Shape Discrimination (PSD)	0.34	> 0.99
Z-position Cut	0.36	0.80
Combined	0.0011	0.77

### 4.3 Event Selection

Neutrino-induced interactions like  $\bar{\nu}_e - e$  are of extremely small cross-section and therefore manifest themselves as “single-hit” (H1) events in only one crystal module uncorrelated to the rest of the system. The H1 events were selected from raw data through selection criteria with CRV, “anti-Compton” multi-hit veto (MHV), and PSD. The CRV and MHV suppressed cosmic-induced background and multiple Compton scattering events from ambient  $\gamma$ -rays, respectively. The selected sample is denoted by H1(CRV) in subsequent discussions. The  $\alpha$  and delay-cascade events from internal radioactivity [35], as well as convoluted events in accidental coincidence, were identified by PSD. To minimize background due to ambient  $\gamma$ -rays, an internal fiducial volume was defined. Events at the outermost layers of the crystal array were rejected, and a Z-position cut of 4 cm from both ends was applied to the target (inner) crystals.

The various parameters in the calibration and selection procedures were measured before the detector were assembled on site. Typically, about 10% of the *in situ* data samples uniformly distributed within a DAQ period were used to provide the fine adjustments. Once obtained, the optimal parameters were applied universally to the rest of the data set. The energy spectra at the successive stages of candidate event selection are depicted in Figure 9.

A summary of the background suppression and signal efficiency factors of the cuts in the energy range of interest (3–8 MeV) are summarized in Table III. The signal efficiencies were derived from the survival fractions of RT events for the CRV and MHV cuts, and with the multi-hit Compton events for the PSD cut. The Z-position efficiency corresponds to a 4 cm cut at both ends and were accounted for in the definition of the fiducial volume.

## 5. BACKGROUND

The candidate event selection procedures of Section 4.3 resulted in a signal-to-background ratio of about 1/30 at

3 MeV. The information on multiplicity, energy, position, cascade event timing and  $\alpha/\gamma$  identification available for every event allowed the residual background to be understood, analyzed and suppressed. In addition, the Reactor ON/OFF comparisons provided an independent handle to the background. These measurements were combined to improve the background evaluation which in turn enhanced the experimental sensitivities.

## 5.1 Background Understanding and Diagnostics

Several diagnostic tools which contribute to the quantitative understanding of the background are discussed in this section. For completeness, all prominent background channels are presented, though many of those are below the  $>3$  MeV energy range relevant to the physics analysis of this measurement.

### 5.1.1 Intrinsic Background

Measurements of intrinsic radiopurity in the CsI(Tl) crystal with *in situ* data were discussed in details in Ref. [35].

The isotope  $^{137}\text{Cs}$  is produced artificially as fission waste from power reactors and atomic weapon tests. Cesium salts are soluble and can easily contaminate the raw materials which produce CsI. The  $^{137}\text{Cs}$  contaminations was measured to be  $(1.7 \pm 0.3) \times 10^{-17}$  g/g, and were uniform across the length of the crystals, as depicted in Figure 8.

The cascade events provided measurements on the naturally-occurring  $^{238}\text{U}$ ,  $^{232}\text{Th}$  and  $^{235}\text{U}$  series, which were  $(0.82 \pm 0.02) \times 10^{-12}$  g/g,  $(2.23 \pm 0.06) \times 10^{-12}$  g/g and  $< 4.9 \times 10^{-14}$  g/g, respectively, assuming secular equilibrium. The  $\beta$ -decays of  $^{208}\text{Tl}$  followed by  $\gamma$ 's in coincidence could in principle lead to background in the signal region. From the measured level of  $^{228}\text{Th}$  in the target, the contribution of this background at 3–5 MeV was evaluated to be only  $\lesssim 11\%$  of the expected  $\bar{\nu}_e$ -e signals.

In addition, trace admixtures of the fission daughter  $^{129}\text{I}$  and of the naturally-occurring  $^{40}\text{K}$  in the raw CsI powder were measured with accelerator mass spectrometry techniques to be  $< 1.3 \times 10^{-13}$  g/g and  $< 2 \times 10^{-10}$  g/g, respectively [36]. Neutron capture on  $^{133}\text{Cs}$  produced  $^{134}\text{Cs}$  at the level of  $\sim 5 \times 10^{-20}$  g/g, as measured with the *in situ* two-hit background discussed in Section 5.1.4.

### 5.1.2 Ambient Radioactivity

The H1 spectra of Figure 9 show several  $\gamma$ -lines, the most prominent ones were those from  $^{137}\text{Cs}$ ,  $^{40}\text{K}$  and

$^{208}\text{Tl}$ . The background dropped by several orders of magnitude beyond the natural radioactivity end-point of 2.6 MeV. The cut-off at 8 MeV corresponded to the end-point of  $\gamma$ -rays emissions following neutron capture. The lines are crucial for energy calibration, system stability monitoring, and background diagnostics. Apart from  $^{137}\text{Cs}$  which is an intrinsic radioactivity, the other sources are external to the CsI(Tl) target. Distributions of the Z-position were heavily attenuated from the edge of the crystals, as illustrated for the case of  $^{40}\text{K}$  in Figure 8.

### 5.1.3 Cosmic Ray Tagging Efficiency

The cosmic-ray tagging efficiency ( $\epsilon_\mu$ ) is the probability that the cosmic-ray induced events actually produce a ‘‘cosmic-ray tag’’ (CRT). The inefficiency ( $1 - \epsilon_\mu$ ) was due to incomplete geometrical coverage and the light collection deficiencies of the large-area scintillator panels.

High energy events above the end-point of (n, $\gamma$ ) energy scale of  $\sim 8$  MeV are all cosmic-ray induced. These events provided a clean sample for  $\epsilon_\mu$  to be measured. For improved experimental control, three-hit events (H3) between 8–14 MeV were selected, and  $\epsilon_\mu$  is given by

$$\epsilon_\mu = \left[ \frac{\text{H3(CRT)}}{\text{H3(Total)}} \right]. \quad (15)$$

The  $\epsilon_\mu$  averaged over all the DAQ periods was measured to be 92%, while the variations among periods were less than 1%.

### 5.1.4 Diagnostics of Two-Hit Background

Multi-hit events were unrelated to neutrino interactions and therefore provided unambiguous diagnostics to the background sources. Displayed in Figure 11 is a scatter plot of two-hit (H2) events after CRV cut. Several features were noted which revealed the nature and locations of the dominant background sources, discussed as follows:

#### 1. $^{208}\text{Tl}$ Induced Pair Production:

The single escape peak following pair production of the  $^{208}\text{Tl}$  2614 keV  $\gamma$ 's can be identified. The Z-position distribution of these events confirmed that the sources were external to the target. As discussed in Section 5.2.2, pair production events are crucial for background evaluation because of their distinctive topologies.

#### 2. $^{60}\text{Co}$ Contaminations:

It was established that the dominant reactor-induced radioactivity in KSNL was  $^{60}\text{Co}$  which existed as dust in the laboratory area [16]. Their contributions varied between

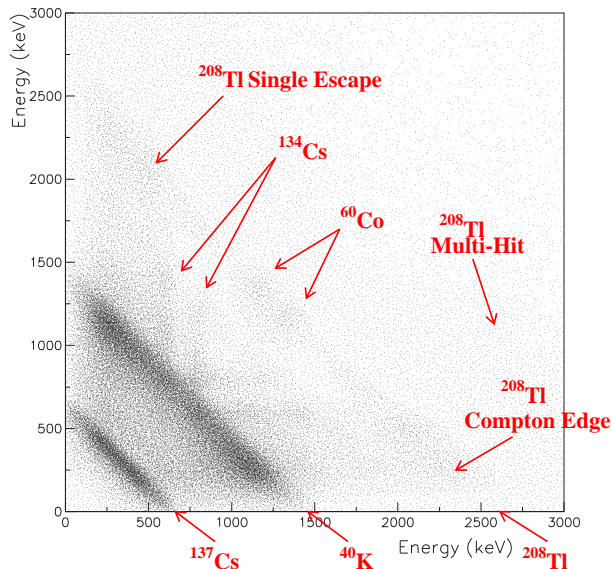


FIG. 11: Scatter plot of H2 events after cosmic-ray veto in 0–3 MeV, showing bands on  $^{60}\text{Co}$ ,  $^{134}\text{Cs}$  and  $^{208}\text{Tl}$  single-escape, as well as the correlated  $\gamma$ 's from  $^{208}\text{Tl}$ .

DAQ periods due to different levels of contaminations during hardware installation.

Events due to the correlated  $\gamma$ 's at energy 1173 keV and 1332 keV from  $^{60}\text{Co}$  can be located in Figure 11. They were uniformly distributed along the Z-position, signifying that some  $^{60}\text{Co}$  dust got *into* the target volume between crystals during installation. The measured contamination level is about  $3 \times 10^{-20} \text{ kg}^{-1}$ . However, the total energy of the  $^{60}\text{Co}$  lines is below the 3 – 5 MeV signal region relevant to this measurement.

**3. Neutron Capture Induced  $^{134}\text{Cs}$ :** Trace amount of  $^{134}\text{Cs}$  ( $\tau_{1/2} = 2.05 \text{ yr}$ ;  $Q = 2.06 \text{ MeV}$ ) was produced by neutron capture on  $^{133}\text{Cs}$  within the CsI(Tl) target. It decays via  $\beta$ -emission together with two  $\gamma$ 's of energy 605 keV and 796 keV in coincidence. These events were tagged in the H2 plot in Figure 11. The intensity distribution is uniform over the length of the crystals, verifying the sources were internal. The measured contamination level is about  $5 \times 10^{-20} \text{ g/g}$ . The Q-value is below the physics analysis threshold and hence these decays would not contribute to the background of this measurement.

**4. Cascade  $\gamma$ -rays from  $^{208}\text{Tl}$ :** Decays of  $^{208}\text{Tl}$  are characterized by several  $\gamma$ -rays emitted in cascade. Coincidences of  $\gamma$ -rays at 510, 583 and 860 keV with the prominent line of 2614 keV can be identified in the H2 scatter plot of Figure 11. The evaluation of the contributions of this channel to H1 events is

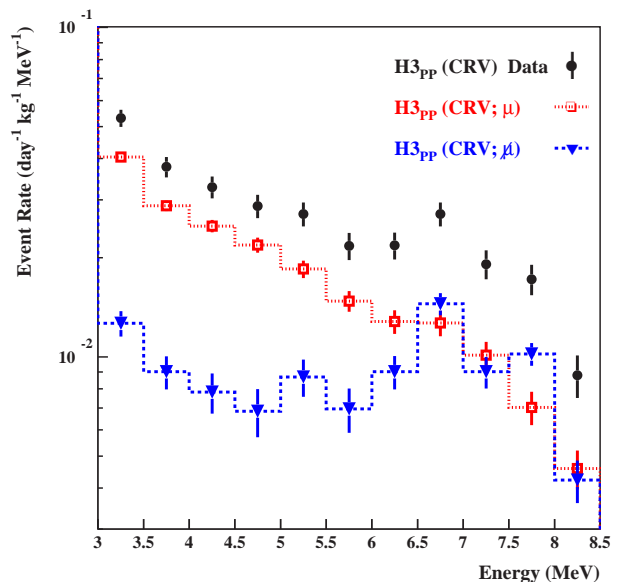


FIG. 12: Three-hit pair production spectra for CRV events, and further differentiating into the cosmic-ray related and unrelated components. After scaling with the known pair production cross-sections, these spectra provide the *in situ*  $\gamma$ -ray background at the detector.

crucial to background suppression, and is addressed in Section 5.2.1.

**5. Neutron Capture on  $^{63}\text{Cu}$ :** The main shielding materials in the vicinity of the target were OFHC copper. Neutron ( $n, \gamma$ ) capture on  $^{63}\text{Cu}$  has relatively large cross-section (4.5 b), giving rise to high energy  $\gamma$ 's at 7637 keV and 7916 keV. These were observed in H1 spectrum shown in the inset of Figure 9.

### 5.1.5 Pair Production Event Samples

Pair production background manifested themselves mostly as three-hit events ( $\text{H3}_{\text{PP}}$ ). They were selected by requiring two crystals each having 511 keV of energy back-to-back to the third one. These samples have distinctive topology not contaminated by other background channels. Coupled with the known energy dependence of the pair production cross-section, these samples provided measurements of the *in situ*  $\gamma$ -spectra, and therefore were crucial for subsequent background evaluation.

The  $\text{H3}_{\text{PP}}$  spectrum for CRV events are displayed in Figure 12. This was produced by the  $\gamma$ -ray background whose contributions to the H1(CRV) signals were evaluated. There were two components to this high energy  $\gamma$ -ray background:

1. cosmic-ray induced events with missing CR-tags,

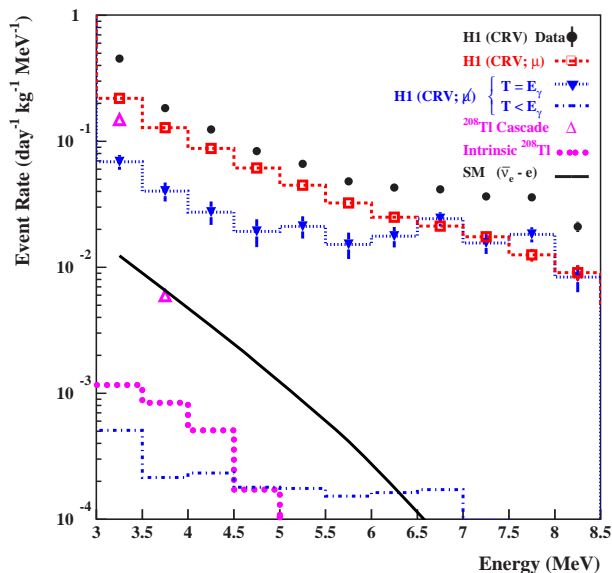


FIG. 13: Measured H1 spectrum and the different background channels evaluated in Section 5.2. The SM  $\bar{\nu}_e$ -e contributions are overlaid.

whose rates are given by

$$H_{3PP}(\text{CRV}; \mu) = \left[ \frac{(1 - \epsilon_\mu)}{\epsilon_\mu} \right] H_{3PP}(\text{CRT}) , \quad (16)$$

where  $\epsilon_\mu$  is the cosmic-ray tagging efficiency measured with Eq. 15, and

2. ambient radioactivity unrelated to cosmic-rays, which can be evaluated with

$$H_{3PP}(\text{CRV}; \mu) = H_{3PP}(\text{CRV}) - H_{3PP}(\text{CRV}; \mu) , \quad (17)$$

also depicted in Figure 12.

## 5.2 Background Evaluation

The experiment focused on the  $3 \text{ MeV} < T < 8 \text{ MeV}$  energy range as the physics analysis window. The  $\bar{\nu}_e$ -e signal region is expected to be at  $\sim 3$ - $5 \text{ MeV}$  due to rapid decrease of the reactor  $\bar{\nu}_e$ -spectra.

The background diagnostics in Section 5.1 demonstrated that convoluted  $\gamma$ -rays from  $^{208}\text{Tl}$ , cosmic-ray events with missing CRV tags, as well as ambient high energy photons could contribute to the H1 background [H1(BKG)]. The experimental design allowed quantitative measurement of these background which resulted in the extraction of the  $\bar{\nu}_e$ -e signal events with good accuracy.

The evaluation of the various background channels is discussed in the following sub-sections. Their contributions are depicted in Figure 13, where the expected SM  $\bar{\nu}_e$ -e spectrum is overlaid for comparison.

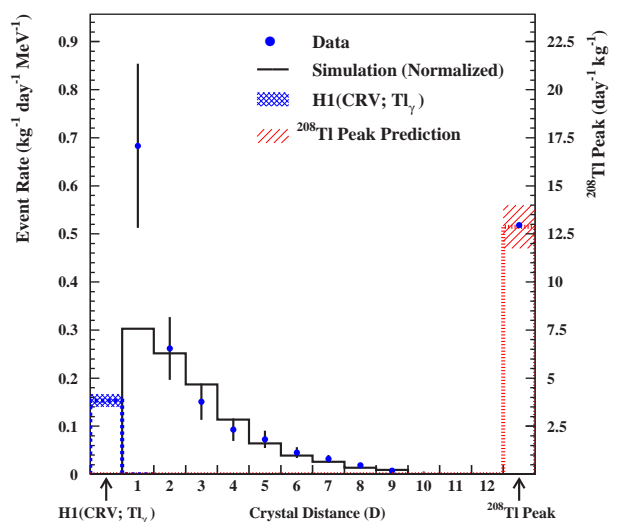


FIG. 14: Comparison of measured H2 correlated events with simulation results on the cascade  $\gamma$ -rays due to  $^{208}\text{Tl}$  decays. The entry H1(CRV;  $\text{Tl}_\gamma$ ) denotes the predicted H1 background produced by two  $\gamma$ 's depositing all energy only in the same crystal. The measured strength of the  $^{208}\text{Tl}$  peak provided consistency cross-checks to the simulations.

### 5.2.1 Cascade $\gamma$ -Rays from $^{208}\text{Tl}$

Decays of  $^{208}\text{Tl}$  are followed by emissions of  $\gamma$ -rays in coincidence, having energy  $E_{\text{Tl}}(1, 2, 3, 4) = 2614.5, 860.56, 583.2$  and  $510.8 \text{ keV}$ , and at intensity ratios of 99, 12.8, 86.2 and 25% per  $^{208}\text{Tl}$ -decay, respectively. Two-fold coincidence manifested as H2 events were identified in the scatter plot of Figure 11. Events with both  $\gamma$ -rays hitting and depositing all energy in the same crystal would become H1 background to the  $\bar{\nu}_e$ -e signals.

The probabilities were studied by full simulations with GEANT software packages [37], incorporating realistic angular correlations and branching ratios for the  $^{208}\text{Tl}$  decays [38]. The sources were located at the PMTs and their voltage dividers, which were the only materials other than OFHC copper and teflon in the vicinity of the target.

The measured H2 distribution of  $E_{\text{Tl}}(1) \oplus E_{\text{Tl}}(2, 3, 4)$  as a function of distance between the two crystals (D) was displayed in Figure 14. The simulation results are overlaid, the normalization of which was fixed by best-fit to the H2 distribution for events with separation more than one crystal ( $D > 1$ ). Excellent agreement with the strength of the  $E_{\text{Tl}}(1)$  single- $\gamma$  H1 peak at 2614 keV was demonstrated. It served as important consistency check and tools for systematic studies. The data point at  $D=1$  denotes H2 events with hits from adjacent crystals. The measured intensity was significantly larger than the expected contributions from correlated  $\gamma$ 's due to  $^{208}\text{Tl}$ . The excess was attributed to multiple Compton scatterings from a single high energy photon.

The entry at  $D=0$ , denoted by  $H1(\text{CRV}; T1_\gamma)$ , corresponds to the prediction of the H1 events having the two  $\gamma$ 's depositing energy exclusively in the same crystal. It was adopted for subsequent background subtraction. The relative intensities to the 2614 keV reference peak, expressed as ratios of  $[E_{T1}(1) \oplus E_{T1}(N)]/E_{T1}(1)$  in H1-events, are 0.13%, 0.33%, and 0.16%, for  $N=2,3,4$ , respectively.

### 5.2.2 Cosmic-Ray Induced Background

Once the cosmic-ray tagging efficiency ( $\epsilon_\mu$ ) was measured with Eq. 15, the cosmic-ray induced H1 background with missing CR tags was derived using

$$H1(\text{CRV}; \mu) = \left[ \frac{(1 - \epsilon_\mu)}{\epsilon_\mu} \right] H1(\text{CRT}) , \quad (18)$$

similar to the  $H3_{\text{PP}}$  channel in Eq. 16.

### 5.2.3 Ambient $\gamma$ -Ray Background

This background channel  $H1(\text{CRV}; \mu^\dagger)$  is due to ambient high energy photons emitted mostly through thermal neutron capture by the surrounding materials. This was derived directly through the  $H3_{\text{PP}}(\text{CRV}; \mu^\dagger)$  spectrum of Figure 12. The sharp cut-off at  $\sim 8$  MeV indicates the dominance of  $(n, \gamma)$  processes.

The background can be further divided into two categories, according to the different methods of evaluation.

#### 1. Full Energy Deposition ( $T = E_\gamma$ ):

The  $\gamma$ -rays lose all its energy within a single crystal through multiple Compton scatterings or pair production with both annihilation photons fully absorbed. The rate is given by

$$H1(\text{CRV}; \mu^\dagger) = \left[ \frac{H3_{\text{PP}}(\text{CRV}; \mu^\dagger)}{H3_{\text{PP}}(\text{CRT})} \right] \cdot H1(\text{CRT}) . \quad (19)$$

The evaluation of  $H3_{\text{PP}}(\text{CRV}; \mu^\dagger)$  followed from Eq. 17.

#### 2. Partial Energy Deposition ( $T < E_\gamma$ ):

The ambient  $\gamma$ 's could undergo single Compton scattering after which the outgoing photons left the detector without further interactions. Only a fraction of the incident energy would be deposited in a single crystal. This background channel was studied with full-scale simulations using the *in situ* cosmic-unrelated  $H3_{\text{PP}}(\text{CRV}; \mu^\dagger)$  spectrum of Figure 12 for flux normalization. For consistency check, the strength of the H1 full energy ( $T = E_\gamma$ ) spectra of Figure 13 was successfully reproduced. The contribution by this channel to  $H1(\text{BKG})$  at 3–5 MeV was only  $\lesssim 5\%$  of the expected SM  $\bar{\nu}_e - e$  signals.

### 5.2.4 Combined Evaluation

It can be derived from Figure 13 that  $\gtrsim 99\%$  of the  $H1(\text{CRV})$  events can be accounted for by the  $\bar{\nu}_e - e$  signals as well as the three dominant background channels, such that:

$$\begin{aligned} H1(\text{CRV}) &= H1(\bar{\nu}_e - e) + H1(\text{BKG}) ; \\ H1(\text{BKG}) &\cong \\ H1(\text{CRV}; T1_\gamma) &+ H1(\text{CRV}; \mu) + H1(\text{CRV}; \mu^\dagger) , \end{aligned} \quad (20)$$

where the three contributions are given by Fig. 14 and Eqs. 18&19, respectively. The sub-dominant terms include intrinsic radiopurity and ambient  $\gamma$ -ray background with partial energy deposition which contributed at the  $\lesssim 0.5\%$  level of  $H1(\text{BKG})$ .

The  $H1(\text{CRV}; T1_\gamma)$  channel was important only in the 3–3.5 MeV energy bin. The other two channels due to high energy  $\gamma$  interactions were dominant over the entire energy range of interest. Their combined contributions were simplified by Eqs. 16,17,18&19, to become:

$$H1(\text{CRV}; \mu) + H1(\text{CRV}; \mu^\dagger) = \left[ \frac{H3_{\text{PP}}(\text{CRV})}{H3_{\text{PP}}(\text{CRT})} \right] \cdot H1(\text{CRT}) . \quad (21)$$

That is, the dominant contribution to  $H1(\text{BKG})$  was related to the  $H3_{\text{PP}}$  sample through a simple ratio of events with and without CR-tags.

## 6. SYSTEMATIC UNCERTAINTIES

A summary of the sources of systematic errors [ $\delta_{\text{sys}}(\text{Source})$ ] and their contributions to the measured  $\xi$ -ratio [ $\Delta_{\text{sys}}(\xi)$ ] is given in Table IV. An uncertainty of 3% was adopted for the evaluation of the high energy reactor  $\bar{\nu}_e$ -spectra. The signal efficiencies for the selection procedures discussed in Section 4.3 were accurately measured with high statistics using the RT events. The fiducial mass uncertainties originated from the Z-position resolution of 1.3 cm.

The systematic effects on background evaluation were studied with event samples unrelated to neutrino interactions accumulated over all DAQ periods. These include data from the Reactor OFF periods as well as those with energy above the 8 MeV end-point of the reactor neutrino spectra. Individual methods were demonstrated to be able to account for the neutrino-unrelated background to certain accuracy levels, which were in turn assigned as the systematic uncertainties of those methods.

#### 1. Reactor ON/OFF Comparison:

The intensity of the  $^{208}\text{Tl}$   $\gamma$ -line allowed the stability of the hardware systems to be monitored and demonstrated to good statistical accuracies. The

TABLE IV: Summary of the sources of systematic errors [ $\delta_{sys}(\text{Source})$ ] and their contributions to the measurement uncertainties [ $\Delta_{sys}(\xi)$ ]. The various components to the signal strength are summed, while those to the background subtraction are averaged.

Sources	$\delta_{sys}(\text{Source})$	$\Delta_{sys}(\xi)$
<b>Signal Strength :</b>		
$\Phi_\nu$ Evaluation	<3%	<0.03
Efficiencies for Neutrino Events	<1.3%	<0.013
Fiducial Target Mass	<4%	<0.04
* Combined (Signal)	—	<0.052
<b>Background Subtraction :</b>		
Reactor OFF Measurement	< 0.4%	<0.06
Background Evaluation		
○H1(CRV; $\text{TI}_\gamma$ )	<3%	<0.08
○H1(CRV; $\mu$ ) + H1(CRV; $\mu\bar{\nu}$ )	< 1%	<0.17
Net	—	<0.19
* Combined (Background)	—	<0.15
Total		<0.16

TABLE V: Stability levels ( $\delta_\pm$ ) of the various neutrino-unrelated channels.

Channels/Period	$\chi^2/\text{dof}$	$\delta_\pm$ (%)
<b><math>^{208}\text{Tl}</math> Intensity :</b>		
II	19/13	0.85
III	38/43	0.61
IV	33/27	0.81
V	8.4/8	0.91
<b>Reactor OFF 3–8 MeV H1(CRV) Rates :</b>		
II	15/14	3.18
III	11/11	3.51
IV	8.1/8	3.60
V	7.2/5	3.22
Combined	—	< 0.4%

window within 3–8 MeV at the Reactor OFF periods consisted exclusively of background and provided an additional monitor. The stability of the measured intensities of the  $^{208}\text{Tl}$   $\gamma$ -line at 2614 keV in Period III relative to the whole-period average is illustrated in Figure 15a. Summary of all results are tabulated in Table V. The good reduced- $\chi^2$  ( $\chi^2/\text{dof}$ ) indicate the data were stable within individual periods. The hardware instability level demonstrated with the combined data is < 0.4%.

## 2. $^{208}\text{Tl}$ Induced $\gamma$ -Ray Cascade Background

The simulation software and the normalizations discussed in Section 5.2.1 were cross-checked by applying them to compare with the measured intensities of the 2614 keV  $\gamma$ -line following  $^{208}\text{Tl}$  decays for all periods, and with the H1 events at 3–5 MeV for only Reactor OFF. The relative deviations between the measured and predicted rates  $[(R_{\text{meas}} - R_{\text{pred}})/R_{\text{meas}}]$  are depicted in Figure 15b, showing consistency with zero [=

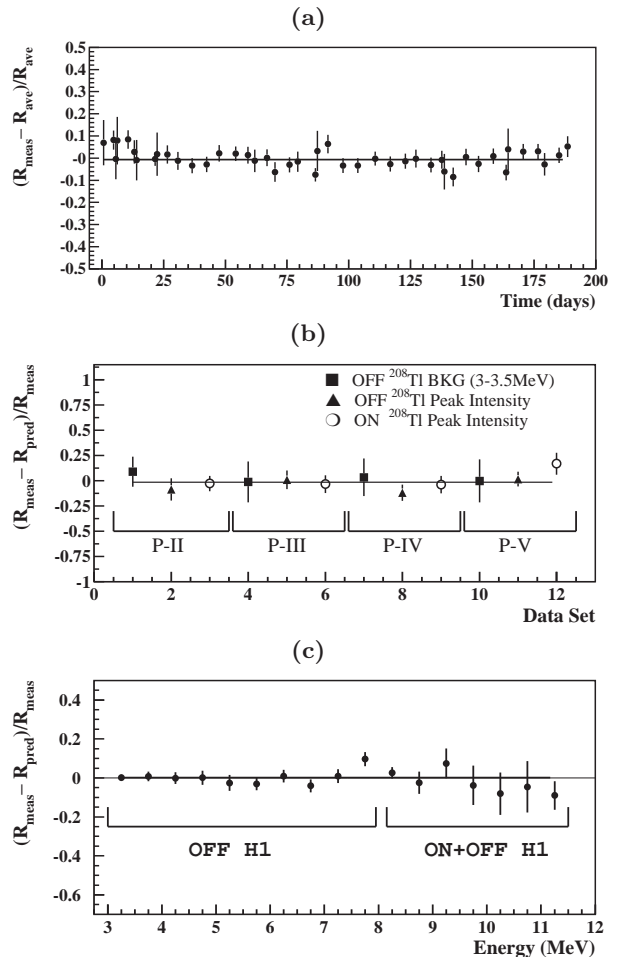


FIG. 15: Data from which the systematic uncertainties were derived: (a) stability of the  $^{208}\text{Tl}$  peak intensities in Period III; (b) comparisons of  $^{208}\text{Tl}$  intensities evaluated by simulations with measured background on neutrino-unrelated data samples, and (c) comparisons of the evaluated H1(CRV;  $\mu$ ) + H1(CRV;  $\mu\bar{\nu}$ ) background channels with measured background on neutrino-unrelated data samples.

$(-0.013 \pm 0.029)$  at  $\chi^2/\text{dof} = 6/11$ ]. The fitting error of 3% represents an upper bound of the systematic uncertainties to the H1(CRV;  $\text{TI}_\gamma$ ) background component.

## 3. Dominant H1(CRV; $\mu$ ) + H1(CRV; $\mu\bar{\nu}$ ) Background:

The evaluations of the H1(CRV;  $\mu$ ) + H1(CRV;  $\mu\bar{\nu}$ ) combined contributions in Eq. 21 were cross-checked with measurements on neutrino-unrelated samples at 3–8 MeV from the Reactor OFF periods and at 8–12 MeV from both ON/OFF periods. The relative deviations  $[(R_{\text{meas}} - R_{\text{pred}})/R_{\text{meas}}]$  were consistent with zero [=  $(0.0021 \pm 0.0081)$  at  $\chi^2/\text{dof} = 14.5/16$ ], as illustrated in Figure 15c for the combined data set.

The fitting error of 1% represents an upper bound of the systematic uncertainties.

The contributions of the individual systematic effects to the  $\bar{\nu}_e$ -e cross-section measurement were then derived. The various  $\delta_{sys}(\text{Source})$  terms were imposed on the data, and the changes introduced on  $\xi$  were the corresponding systematic uncertainties  $\Delta_{sys}(\xi)$  listed in Table IV.

## 7. PHYSICS RESULTS

Intermediate results of the experiment were previously reported [39]. The final physics results presented in this section are based on the complete data set, and include contributions from systematic uncertainties, as well as improvements in the background evaluation.

### 7.1 Formulation

The experimentally measured rates for neutrino events [ $R_{expt}(\nu)$ ] in Eq. 7 are given by:

$$R_{expt}(\nu) = R_{H1}(\text{ON}) - R_{H1}(\text{BKG}) \quad , \quad (22)$$

where  $R_{H1}(\text{ON})$  is the measured H1(CRV) spectra for Reactor ON data, and  $R_{H1}(\text{BKG})$  is the background derived from the statistical average of two different measurements: (1) Reactor OFF data, and (2) sum of the dominant and sub-dominant background contributions to H1(BKG) in both the Reactor ON and OFF periods, the derivations of which are discussed in Section 5.2.4.

Data from the four independent DAQ periods were used, combining to give a total of 29882(7369) kg-day of fiducial mass exposure during Reactor ON(OFF), respectively. The adopted analysis window is 3–8 MeV spread out uniformly over  $N_{bin} = 10$  energy bins.

### 7.2 Cross-Section

The cross-section ratio  $\xi$  defined in Eq. 7 was derived with a minimum- $\chi^2$  fit, defined by

$$\chi^2 = \sum_{i=1}^{N_{bin}} \left\{ \frac{[R_{expt}(i) - \xi \cdot R_{SM}(i)]^2}{\Delta_{stat}(i)^2} \right\} \quad , \quad (23)$$

where  $R_{SM}(i)$  and  $R_{expt}(i)$  are SM-expected and measured event rates at  $i^{th}$  bin, respectively, and  $\Delta_{stat}(i)$  is the corresponding statistical error of the measurement.

As cross-check, identical procedures were applied to the combined Reactor OFF data [ $R_{H1}(\text{OFF})$ ], in which case only the predicted background was subtracted to

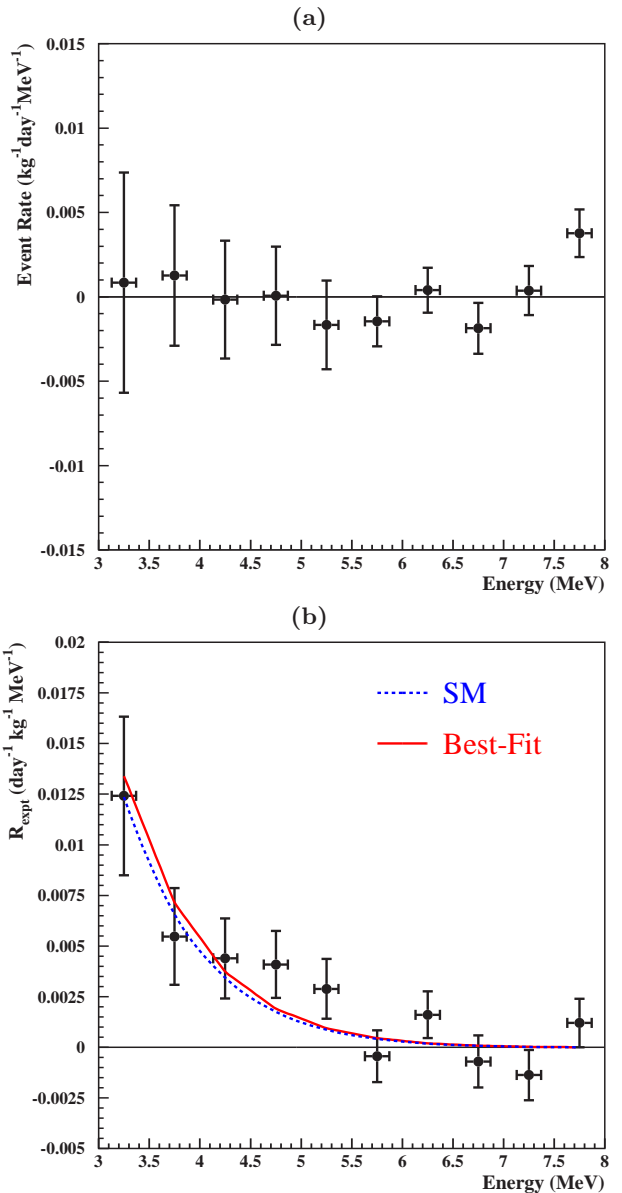


FIG. 16: (a) The residual spectrum [ $R_{H1}(\text{OFF}) - R_{pred}(\text{OFF})$ ] with combined Reactor OFF data. The best-fit to SM effects is consistent with  $\xi = 0$ . (b) The combined residual spectrum [ $R_{expt}(\nu) = R_{H1}(\text{ON}) - R_{H1}(\text{BKG})$ ] in the 3 – 8 MeV energy region. The blue and red lines correspond to the SM expectations and to the best-fit of the data, respectively.

provide the residual spectrum displayed in Figure 16a. Best-fit with Eq. 23 gave

$$\xi(\text{OFF}) = 0.03 \pm 0.36(\text{stat}) \quad (24)$$

at  $\chi^2/\text{dof}=10.3/9$ , demonstrating good overall systematic control of the background subtraction procedures.

Combining all Reactor ON and OFF data from all periods and adopting the systematic uncertainties listed in

TABLE VI: Summary of the measured values of  $\xi$  and  $\chi^2/\text{dof}$  over individual DAQ periods, as well as with the different background subtraction schemes in the total data set.

	$\xi$	$\chi^2/\text{dof}$
<u>Individual Period :</u>		
II	$1.15 \pm 0.55 \pm 0.17$	8.5/9
III	$1.03 \pm 0.43 \pm 0.20$	8.3/9
IV	$1.18 \pm 0.36 \pm 0.19$	7.3/9
V	$0.97 \pm 0.42 \pm 0.20$	9.9/9
<u>All Periods Background Subtraction :</u>		
Measurement Reactor OFF	$1.25 \pm 0.43 \pm 0.08$	7.4/9
Evaluation Reactor OFF	$1.33 \pm 0.37 \pm 0.22$	6.9/9
Evaluation Reactor ON	$0.78 \pm 0.33 \pm 0.20$	10.3/9
Combined	$1.08 \pm 0.21 \pm 0.16$	8.7/9

Table IV, the ratio

$$\xi = 1.08 \pm 0.21(\text{stat}) \pm 0.16(\text{sys}) \quad (25)$$

at  $\chi^2/\text{dof}=8.7/9$  was derived following Eq. 23. The measured  $\bar{\nu}_e-e$  cross-section was consistent with the SM prediction.

The residual and best-fit spectra are depicted in Figure 16b. The  $\xi$  ratios derived from individual periods as well as with background subtraction by different methods are tabulated in Table VI. The consistent distributions of the best-fit values and their errors as well as the appropriate range of  $\chi^2/\text{dof}$  indicate robustness of the analysis procedures. These results represent a probe to SM at  $Q^2 \sim (3 \times 10^{-6}) \text{ GeV}^2$  and improve over those from previous reactor neutrino experiments [7–10].

### 7.3 Electroweak Parameters

The constraints on the coupling constants ( $g_V, g_A$ ) were derived by a minimum- $\chi^2$  two-parameter fit on Eq. 3, with a formulation similar to that of Eq. 23. The allowed regions are presented in Figure 17. Results from the accelerator experiment with  $\nu_e$  [6] are overlaid. The complementarity of the  $\nu_e-e$  and  $\bar{\nu}_e-e$  processes is readily seen.

The weak mixing angle was derived with best-fit on Eq. 5, giving

$$\sin^2\theta_W = 0.251 \pm 0.031(\text{stat}) \pm 0.024(\text{sys}) \quad (26)$$

at  $\chi^2/\text{dof}=8.7/9$ , in excellent agreement with the SM value of  $\sin^2\theta_W(\text{SM}) = 0.23867 \pm 0.00016$  at this low  $Q^2 (< 10^{-4}\text{GeV}^2)$  range [40]. The combined uncertainty of  $\pm 0.039$  from this measurement is less than that from the LSND accelerator  $\nu_e-e$  experiment of  $\pm 0.051$ . The improvement is due to the enhancement factors favoring  $\bar{\nu}_e-e$  processes, as indicated in Eq. 9.

The interference term was probed using Eq. 8. The best-fit value of the sign-parameter  $\eta$  is

$$\eta = -0.92 \pm 0.30(\text{stat}) \pm 0.24(\text{sys}) \quad (27)$$

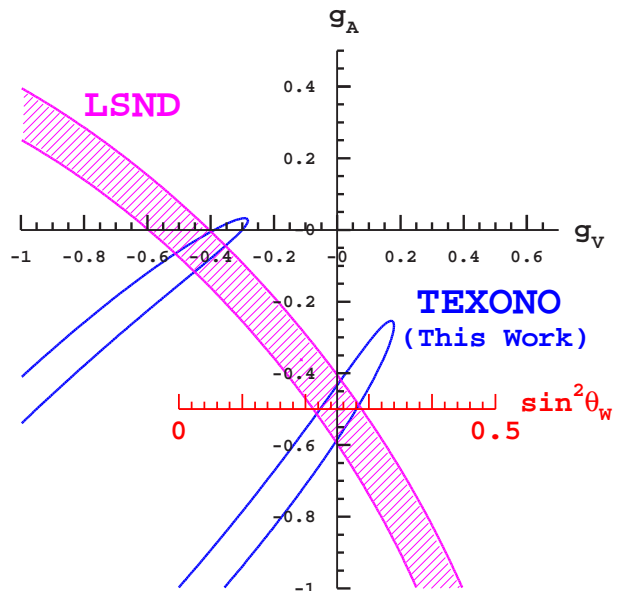


FIG. 17: Best-fit results in ( $g_V, g_A$ ) space and in the  $\sin^2\theta_W$  axis from this experiment on  $\bar{\nu}_e-e$  and the LSND experiment on  $\nu_e-e$ . The allowed regions are defined by their corresponding statistical uncertainties.

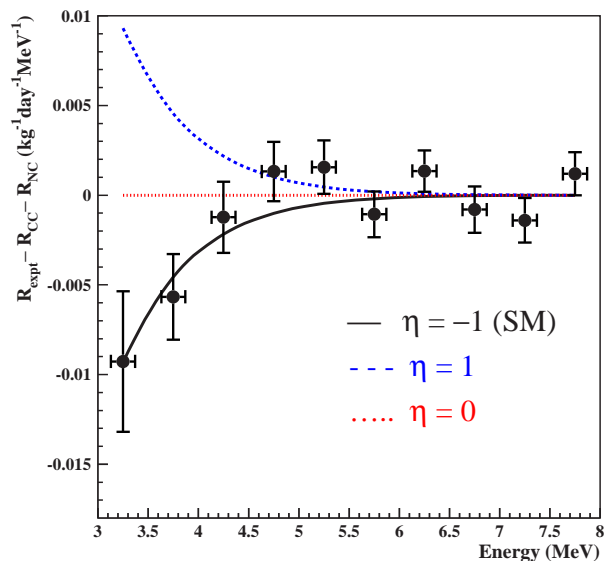


FIG. 18: The measurement of interference term from best-fit to the data in the 3–8 MeV energy range. The solid line corresponds to the SM expectation of  $\eta = -1$ .

at  $\chi^2/\text{dof}=8.8/9$ . The residual spectrum showing ( $R_{\text{expt}} - R_{\text{CC}} - R_{\text{NC}}$ ) is displayed in Figure 18, with the expected spectra for  $\eta = 0, \pm 1$  overlaid. The results verified destructive interference in the SM  $\bar{\nu}_e-e$  interactions.

## 7.4 Neutrino Electromagnetic Properties

To include possible effects due to  $\mu_\nu$  and  $\langle r_{\bar{\nu}_e}^2 \rangle$ , the expression of Eq. 22 was modified to

$$R(\mu_\nu; \langle r_{\bar{\nu}_e}^2 \rangle) = R_{\text{H1}}(\text{ON}) - [R_{\text{SM}}(\nu) + R_{\text{H1}}(\text{BKG})] . \quad (28)$$

The non-standard interaction parameter  $\langle r_{\bar{\nu}_e}^2 \rangle$  as defined in Eq. 11 was measured to be

$$\langle r_{\bar{\nu}_e}^2 \rangle = [0.61 \pm 1.30(\text{stat}) \pm 1.01(\text{sys})] \times 10^{-32} \text{ cm}^2 \quad (29)$$

at  $\chi^2/\text{dof}=8.7/9$ . This can be translated to bounds of

$$-2.1 \times 10^{-32} \text{ cm}^2 < \langle r_{\bar{\nu}_e}^2 \rangle < 3.3 \times 10^{-32} \text{ cm}^2 \quad (30)$$

at 90% confidence level, an improvement over the current limits by the LSND experiment with  $\nu_e$ -e [6]:  $-2.97 \times 10^{-32} \text{ cm}^2 < \langle r_{\bar{\nu}_e}^2 \rangle < 4.14 \times 10^{-32} \text{ cm}^2$ .

Similarly, the best-fit value for  $\mu_\nu^2$  is

$$\mu_\nu^2 = [0.42 \pm 1.79(\text{stat}) \pm 1.49(\text{sys})] \times 10^{-20} \mu_{\text{B}}^2 \quad (31)$$

at  $\chi^2/\text{dof}=8.7/9$ , which corresponds to a limit of the  $\bar{\nu}_e$  neutrino magnetic moment of

$$\mu_{\bar{\nu}_e} < 2.2 \times 10^{-10} \mu_{\text{B}} \quad (32)$$

at 90% confidence level. This is, however, less stringent than the best published limit of  $\mu_{\bar{\nu}_e} < 0.74 \times 10^{-10} \mu_{\text{B}}$  with germanium detector at  $\sim 10$  keV threshold [16].

## 8. SUMMARY AND PROSPECTS

We report in this article an improved measurement of reactor  $\bar{\nu}_e$  with the atomic electrons at the  $Q^2 \sim 10^{-6} \text{ GeV}^2$  range. Complementary and comparable sensitivities on the SM electroweak parameters were achieved as those measurements with accelerator  $\nu_e$  at higher  $Q^2$ .

The detector concept allowed complete three-dimensional event reconstruction, with which we demonstrated that the background above 3 MeV could be identified, studied and accounted for to the level of  $\sim 1\%$  accuracy. The background understanding and subtraction enhanced the experimental sensitivities beyond the conventional Reactor ON-OFF comparisons.

The sensitivities can be further enhanced. As illustrations, the projected improvement under various realistically achievable assumptions are summarized in Table VII. Electromagnetic calorimeters using CsI(Tl) with tens of tons of mass have been constructed, such that the target mass is easily expandable. As shown in Figure 13, the dominant background above 3 MeV were all external to the target scintillator. Accordingly, they will be attenuated effectively through self-shielding in a target

TABLE VII: Projected statistical sensitivities on  $\xi$  and  $\sin^2\theta_{\text{W}}$  under various realistically achievable improvement to the experiment.

Improvement	$\Delta_{\text{stat}}(\xi)$	$\Delta_{\text{stat}}[\sin^2\theta_{\text{W}}]$
This Work	0.21	0.031
Improved Feature :		
A. $\times 10$ Data Strength	0.07	0.010
B. Background Reduction		
B1: $>99\%$ Cosmic-Ray Efficiency	0.12	0.018
B2: $\times \frac{1}{10}$ Reduction in Ambient & $^{208}\text{Tl}$ $\gamma$ 's	0.16	0.024
* With Both B1+B2	0.05	0.007
All Features A+B1+B2 Combined	0.015	0.0022

with bigger mass. The incorporated features listed in Table VII correspond to 10 times increase in data strength and  $>10$  times suppression in background. The statistical accuracies can be improved to about 1.5% and 0.9% for  $\xi$  and  $\sin^2\theta_{\text{W}}$ , respectively.

As indicated in Table IV, the systematic errors on background subtraction are related to the actual background level, such that they will also contribute to  $\Delta_{\text{sys}}(\xi)$  at the  $\lesssim 2\%$  level under the assumption of Table VII. Modest improvement on the evaluation of reactor neutrino spectra will attain similar accuracy. To eliminate the errors in fiducial mass, active light guides with a different scintillating crystal can be coupled to both ends of the CsI(Tl) target crystal. A good candidate is the pure CsI crystal. The vast difference in the scintillation decay times ( $\sim 10$  ns versus  $\sim 1000$  ns for CsI and CsI(Tl), respectively) [30] makes the definition of an inner target volume simple and exact using PSD techniques.

The projected sensitivities of such experiments are similar to those estimated with a large liquid scintillator target [41], and can complement the  $\sin^2\theta_{\text{W}}$  measurements with the high energy accelerator experiments. In particular, these experiments can probe the anomalous NuTeV results [15] at comparable sensitivities but with a different neutrino interaction channel and at a low  $Q^2$  [42].

## ACKNOWLEDGMENTS

The authors are indebted to the many colleagues who made this experiment possible. The invaluable contributions by the technical staff of our institutes and of the Kuo-Sheng Nuclear Power Station are gratefully acknowledged. The veto scintillators loan from the CYGNUS Collaboration is much appreciated. We appreciate comments from Prof. R. Shrock on neutrino charge radius. This work is supported by fundings provided by the National Science Council and the Academia Sinica, Taiwan under various contracts, the National Science Foundation, China, under contract 19975050, as well

as TUBITAK, Turkey, under contract 108T502.

---

\* Corresponding Author: htwong@phys.sinica.edu.tw;  
Tel:+886-2-2789-9682; FAX:+886-2-2788-9828.

- [1] B. Kayser, Phys. Lett. **B 667**, 163 (2008), and references therein.
- [2] J. Erler and P. Langacker, Phys. Lett. **B 667**, 125 (2008), and references therein.
- [3] J. Panman, in *Precision tests of the standard electroweak model*, ed. P. Langacker, 504-544, World Scientific (1995); W.J. Marciano and Z. Parsa, J. Phys. **G 29**, 2629 (2003).
- [4] J. Dorenbosch et al., Z. Phys. **C 41**, 567 (1989); L.A. Ahrens et al., Phys. Rev. **D 41**, 3297 (1990); P. Vilian et al., Phys. Lett. **B 335**, 246 (1994).
- [5] R.C. Allen et al., Phys. Rev. **D 47**, 11 (1993).
- [6] L.B. Auerbach et al., Phys. Rev. **D 63**, 112001 (2001).
- [7] F. Reines, H.S. Gurr, H.W. Sobel, Phys. Rev. Lett. **37**, 315 (1976).
- [8] G.S. Vidyakin et al., JETP Lett. **55**, 206 (1992).
- [9] A.I. Derbin et al., JETP Lett. **57**, 796 (1993).
- [10] C. Amsler et al., Nucl. Instr. and Meth. **A 396**, 115 (1997); Z. Daraktchieva et al., Phys. Lett. **B 615**, 081601 (2005).
- [11] J.P. Cravens et al., Phys. Rev. **D 78**, 032002 (2008); B. Aharmim et al. Phys. Rev. **C 75**, 045502 (2007).
- [12] B. Kayser et al., Phys. Rev. **D 20**, 87 (1979).
- [13] P. Vogel and J. Engel, Phys. Rev. **D 39**, 3378 (1989).
- [14] J. Barranco et al., Phys.Lett.**B 662**, 431-435,(2008).
- [15] G.P. Zeller et al., Phys. Rev. Lett. **88**, 091802 (2002) [Erratum-ibid. **90**, 239902 (2003)].
- [16] H.B. Li et al., Phys. Rev. Lett. **90**, 131802 (2003); H.T. Wong et al., Phys. Rev. **D 75**, 012001 (2007), and references therein.
- [17] B. Kayser, Phys. Rev. **D 26**, 1662 (1982); J.F. Nieves, Phys. Rev. **D 26**, 3152 (1982); R. Shrock, Nucl. Phys. **B 206**, 359 (1982).
- [18] H.T. Wong, Nucl. Phys. **B (Procs. Suppl.) 143**, 205 (2005); H.T. Wong and H.B. Li, Mod. Phys. Lett. **A 20**, 1103 (2005).
- [19] B.W. Lee and R.E. Shrock, Phys. Rev. **D 16**, 1444 (1977); K. Fujikawa and R. Shrock, arXiv:hep-ph/0303188 (2003); K. Fujikawa and R. Shrock, Phys. Rev. **D 69**, 013007 (2004).
- [20] J. Bernabeu et al., Phys. Rev. **D 62**, 113012 (2000); J. Bernabeu, J. Papavassiliou and J. Vidal, Phys. Rev. Lett. **89**, 101802 (2002), [Erratum-ibid. **89**, 229902 (2002)]; J. Bernabeu, J. Papavassiliou and J. Vidal, arXiv:hep-ph/0303202 (2003).
- [21] P. Vogel and A. Piepke, Phys. Lett. **B 667**, 522 (2008), and references therein.
- [22] A.G. Beda et al., arXiv:hep-ex/0906.1926 (2009).
- [23] H.T. Wong, Mod. Phys. Lett. **A 19**, 1207 (2004).
- [24] H.B. Li and H.T. Wong, J. Phys. G: Nucl. Part. Phys.**28**, 1453 (2002).
- [25] Y. Declais et al., Phys. Lett. **B 338**, 383 (1994).
- [26] B. Achkar et al., Phys. Lett. **B 374**, 243 (1996).
- [27] H.T. Wong et al., Astroparticle Phys. **14**, 141 (2000).
- [28] H.B. Li et al., Nucl. Instr. and Meth. **A 459**, 93 (2001).
- [29] H.S. Lee et al., Phys. Lett. **B 633**, 201 (2006).
- [30] Y. Liu et al., Nucl. Instr. and Meth. **A 482**, 125 (2002).
- [31] S.C. Wu et al., Nucl. Instr. and Meth. **A 523**, 116 (2004).
- [32] S.T. Lin et al, Phys. Rev. **D 79**, 061101(R) (2009).
- [33] W.P. Lai et al., Nucl. Instr. and Meth. **A 465**, 550 (2001).
- [34] Q. Yue et al., Nucl. Instr. and Meth. **A 511**, 408 (2003).
- [35] Y.F. Zhu et al., Nucl. Instr. and Meth. **A 557**, 490 (2006).
- [36] K.J. Dong et al., Nucl. Instr. and Meth. **B 259**, 271 (2007); K.J. Dong et al., Nucl. Instr. and Meth. **A 582**, 381 (2007).
- [37] GEANT, Detector Description and Simulation Tool, CERN (1993).
- [38] L.C. Biedenharn and M.E. Rose, Rev. Mod. Phys. **25**, 3 (1953).
- [39] M. Deniz and H.T. Wong, arXiv:hep-ex/0810.0809 (2008).
- [40] J. Erler and M.J. Ramsey-Musolf, Phys. Rev. **D 72**, 073003 (2005).
- [41] J.M. Conrad, J.M. Link, and M.H. Shaevitz, Phys. Rev. **D 71**, 073013 (2005).
- [42] J.L. Rosner, Phys. Rev. **D 70**, 037301 (2004).